



Effects of phonon pore scattering and pore randomness on effective conductivity of porous silicon

Jae Dong Chung¹, Massoud Kaviany*

Department of Mechanical Engineering and Applied Mechanics, The University of Michigan, Ann Arbor, MI 48109-2125, USA

Received 4 January 1999; received in revised form 10 April 1999

Abstract

The observed low effective thermal conductivity of porous silicon makes for its convenient fabrication and integration as a thermal insulation layer in microelectronics. The observed average pore size is controlled by the etching process and ranges between 1 and 100 nm, which on the low end is much less than the bulk phonon mean-free path. This low effective conductivity, i.e., low effective phonon mean-free path, can be explained with the inclusion of the effects of the phonon pore scattering and the pore randomness. The available two-dimensional porous silicon pore-network simulations are used along with the Boltzmann transport equation to determine the effective conductivity. It is shown that the hindering effect of the phonon pore scattering (due to reflection from the solid-pore interface) is significant for small pore size. Also, due to the dendritic structure of the pores, the hindering effect of the pore-network randomness is significant. The predictions are compared with the existing experiments and a good agreement is found. © 1999 Elsevier Science Ltd. All rights reserved.

1. Introduction

Porous silicon layers are formed on the surface of locally or wholly doped silicon wafers. It can also be formed away from the wafer surface by proper, distributed doping. The etching is by anodic dissolution (i.e., electrochemical etching) of the monocrystalline, impurity-doped silicon in aqueous, hydrofluoric acid (HF) solutions. The surface, porous-silicon layer is depicted in Fig. 1. Due to the pore morphology, the effective conductivity is not isotropic and a preferential conduction heat flow occurs along the y -direction. For the surface,

porous layer shown, the porous-layer thickness δ may be as small as a few micron and as large as desired (i.e., up to a few hundred micron). Micrograph of a typical porous silicon surface is shown in Fig. 2. Due to its photoluminescence capability and having physical properties greatly different from the bulk material (such as permeability, low effective thermal conductivity, and low density), porous silicon is a promising material in silicon-based integrated circuits and devices. As an example, many thermal sensors operate are based on the measurement of a small amount of thermal energy. This minute amount of energy must cause a relatively large temperature change in the sensing medium. Then this medium must be small and well isolated from its surroundings and a porous-silicon layer can be used. Although complete backside etching is also possible for insulation, it has a mechanical vulnerability disadvantage compared to porous-silicon layer. Other applications, and the current knowledge about porous silicon, are reviewed by Canham [1].

* Corresponding author. Tel.: +1-313-936-0402; fax: +1-313-647-3170.

E-mail address: kaviany@umich.edu (M. Kaviany)

¹ *Permanent address:* Institute of Advanced Machinery and Design, Seoul National University, Seoul, 151-742, South Korea.

Nomenclature

a	lattice constant	λ_p	phonon mean-free path (m)
\mathbf{a}_p	phonon acceleration vector (m/s^2)	λ	carrier wavelength (\AA)
A_e, A_w	control volume face areas normal to the x -coordinate	μ	directional cosine
B_n, B_s	control volume face areas normal to the y -coordinate	ξ	directional cosine
c	speed of light (m/s)	σ_{SB}	Stefan–Boltzmann constant for phonon ($\text{W/m}^2 \text{K}^4$)
ρc	volumetric heat capacity ($\text{J/m}^3 \text{K}$)	σ_a	absorption coefficient (m^{-1})
d	pore size (m)	σ_{ex}	extinction coefficient (m^{-1})
D	density of states (m^{-3})	σ_s	scattering coefficient (m^{-1})
f	statistical distribution function	τ	relaxation time (s)
h_p	Planck's constant	ω	angular frequency of phonon (s^{-1})
I	phonon intensity ($\text{W/m}^2 \text{sr}$)	Φ	phase function
k	thermal conductivity (W/m K)		
\mathbf{K}	thermal conductivity tensor (W/m K)	<i>Superscripts</i>	
l	unit cell linear dimension (m)	+	upper hemisphere direction
L	length (m)	–	lower hemisphere direction
M	total number of ordinate direction	<i>Subscripts</i>	
$\hat{\mathbf{n}}$	normal vector	f	fluid
p	interface scattering parameter	δ	location $y = \delta$
q	heat flux (W/m^2)	m	angular index
R_d	diffusive reflectivity	n, s, e, w	compass direction
S	source term	p	phonon
t	time (s)	p	control volume center point
T	temperature (K)	s	solid or scattering
T_d	diffusive transmissivity	0	location $y = 0$
u_p	speed of sound (m/s)	1	medium 1
ΔV	volume (m^3)	2	medium 2
w_m	angular weights	12	from medium 1 into medium 2
x	coordinate along the porous silicon layer (m)	21	from medium 2 into medium 1
y	coordinate across the porous silicon layer (m)		longitudinal
		\perp	transverse
<i>Greek symbols</i>		<i>Other symbol</i>	
δ_r	mean interface roughness (m)	$\langle \rangle$	volume averaged value
ε	porosity		

The low effective thermal conductivity of porous silicon is expected to be due to the low-dimensionality of the pore walls. This can result in the domination of pore-surface scattering over the intra-solid attenuation. The low conductivity is also due to the tortuous solid conduction path and the presence of a low conductivity gas (i.e., air) in the pores. The random pore structure (i.e., pore morphology), which varies greatly with the wafer-etching conditions, is relatively well documented. Simulations of the pore structure has also been attempted using various models (namely the diffusion-limited and the kinetic-limited models), and good qualitative agreements have been found with the observations. Measurements of the effective thermal

conductivity of porous silicon have also been made for several different wafer-etching conditions and also after post-etching oxidation.

The Fourier treatment of the effective conductivity tensor (\mathbf{K}), is made by averaging the energy equation over an elementary volume representing the porous medium. When the porous medium has a periodic structure, successful predictions can be made [2]. Recent analytical solutions for periodic structures include that of Bauer [3] for isotropic-periodic, and Lee and Yang [4] for anisotropic-periodic structures. As evident in Fig. 1, porous silicon shows a strong anisotropy and also it is expected that simple, unit-cell based representations will not be realistic and effective.

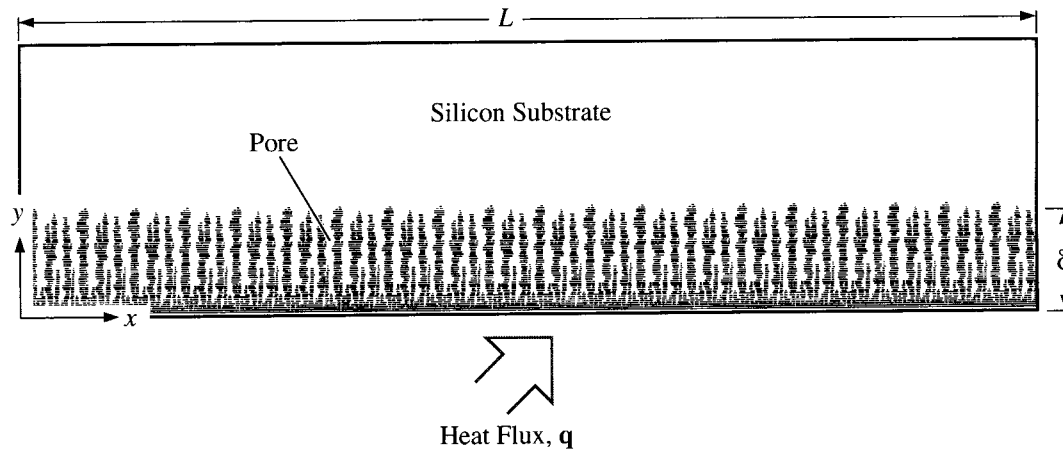


Fig. 1. A schematic of porous silicon layer considered.

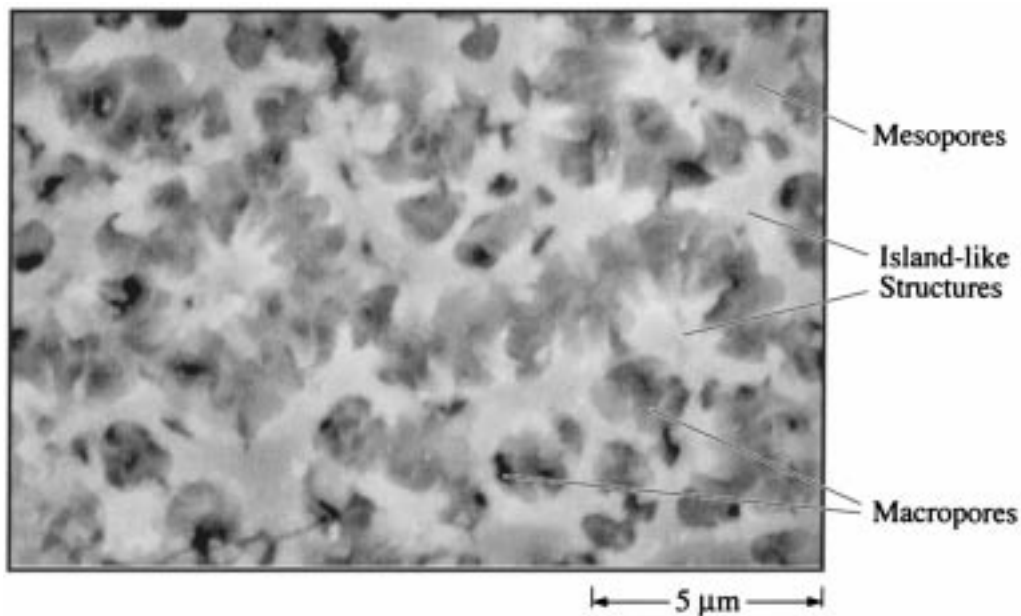


Fig. 2. SEM (top view) of a surface porous layer etched in p^- silicon wafer.

Kaviany [5] provides a review along with a number of correlations for the effective conductivity and their conditions of applicability.

In direct simulation of the effective conductivity tensor rather than imposing a prescribed, simple structure, the pore structure can be scanned from micrographs (two- and three-dimensional structures). This has been done by Nishioka et al. [6] for porous iron (sintered iron particles). The two-dimensional computational

grid consists of the same number of pixels as the scanned image. Bakker [7] also discusses the importance of the inclusion of the actual morphology.

Other than the pore morphology, the size effect and the chemical changes (such as oxidization), also influence $\langle \mathbf{K} \rangle$. The pore-wall length scale of porous silicon can be small compared to the bulk phonon mean-free path λ_p . Then, the silicon-pore interface phonon scattering becomes important. This causes a decrease in

the effective phonon mean-free path [8]. This reduction in $\langle \mathbf{K} \rangle$ becomes more pronounced with a decrease in the ratio of the average pore-wall thickness to the bulk mean-free path.

The oxidization of porous silicon (which is rapid due to the availability of a large specific surface area) for the mesoporous silicon is examined by Drost et al. [9], where they show that $\langle \mathbf{K} \rangle$ decreases upon oxidation. This is because, at room temperature, bulk thermal conductivity of pure silicon is about 149 W/m K and that of silicon oxide is about 1.5 W/m K. Benedetto et al. [10] and Gesele et al. [11] have not addressed the oxidization in the discussion of their experimental results.

Here we use existing pore-network simulations for porous silicon and the Boltzmann transport equation for phonons, to allow for the effects of the pore randomness, low dimensionality of the pore wall, and the pore-surface scattering. We also compare the predicted results with those obtained using the bulk conductivity and the Fourier law (i.e., no low dimensionality), and those based on the unit-cell models (i.e., no randomness). Finally, we compare the predictions with the available experiments.

2. Pore network

The morphology of porous-silicon layers is designated by the average porosity $\langle \varepsilon \rangle$, the average pore size $\langle d \rangle$, the pore-size distribution, and the pore geometry. A wide variety of morphologies is achievable depending on the surface crystal plane orientation, impurity type, electrical resistivity of the doped silicon, and the electrochemical parameters such as HF concentration, electrical current density, anodization time, front- and back-side irradiation, and temperature. The pore size can be controlled over three orders of magnitude from nanometers to micrometers and the average porosity of the obtained layer $\langle \varepsilon \rangle$ can be tuned from 0.10 to 0.90. The porosity decreases substantially upon oxidation.

The pore morphology is characterized by the presence of mesopore and macropore structures. The geometry of the mesopore structures can be divided into columnar (i.e., anisotropic) and equiaxed (i.e., isotropic). For the p^- -type silicon wafers, $\langle d \rangle$ is generally small and the structure is equiaxed. For the p^+ -type, $\langle d \rangle$ is larger and the pores are more columnar. The trend is basically the same for the n -type silicon [12,13]. The n -type silicon etched with a light illumination is very similar in structure to the p -type silicon. However, the pore diameters in n -type silicon (100 nm or more) are considerably larger than the p -type silicon. An overview of the different morphologies is given in Ref. [14]. Fig. 3 presents a summary of the

above morphological characteristics of the porous silicon layers with the impurity as a variable.

The mechanisms of formation of porous silicon has been extensively studied, but is not completely clear. The diffusion-limited model, proposed by Smith et al. [15], is one of the accepted models for the pore formation. It explains pore formation from the diffusion of an electroactive species, such as holes and electrons, to or from the silicon interface. The computer simulations of the porous silicon formation using the diffusion-limited model, shows a striking resemblance to the micrographs. Fig. 4 is a typical pore structure obtained from the diffusion-limited simulation. The figure also shows the representative elementary volumes chosen. Each axis gives the grid number in that direction.

A typical pore-size distributions obtained by nitrogen adsorption, for the pore structure in Fig. 2, is shown in Fig. 5(a). The diffusion-limited model does not address the pore size. The dimensionless pore size distribution for the pore network of Fig. 4 is shown in Fig. 5(b). The average pore size for simulation can be estimated using this similarity, although depending on the dopant used and the etching applied, different pore distributions are obtained.

3. Energy equation with Fourier law

On a macroscopic scale, conductive heat transfer can be accurately represented by the Fourier law and energy equation as

$$\mathbf{q} = -k\nabla T, \quad \nabla \cdot \mathbf{q} = 0. \quad (1)$$

From the kinetic theory, the thermal conductivity of non-metallic solids can be related to their other physical properties as [8]

$$k = \rho c_p u_p \lambda_p / 3, \quad (2)$$

where ρc_p is the lattice heat capacity, u_p is the phonon speed, and λ_p is the phonon mean-free path. Although the laws of macroscopic heat transport are well known, there exist regimes of size and temperature where such laws are no longer applicable [16–18]. Recent experiments show that the phonon scattering at the interface of small, dissimilar materials is considerable enough to reduce the heat transfer rate [19–21].

Here, for prediction of $\langle \mathbf{K} \rangle$, we begin by using the bulk thermal conductivity of silicon along with the Fourier treatment. Then the effect of the pore morphology of porous silicon on the effective thermal conductivity is examined. In the next section, the Boltzmann treatment is applied to include the low-dimensionality effect.

Schematic diagrams of two-dimensional unit cell,

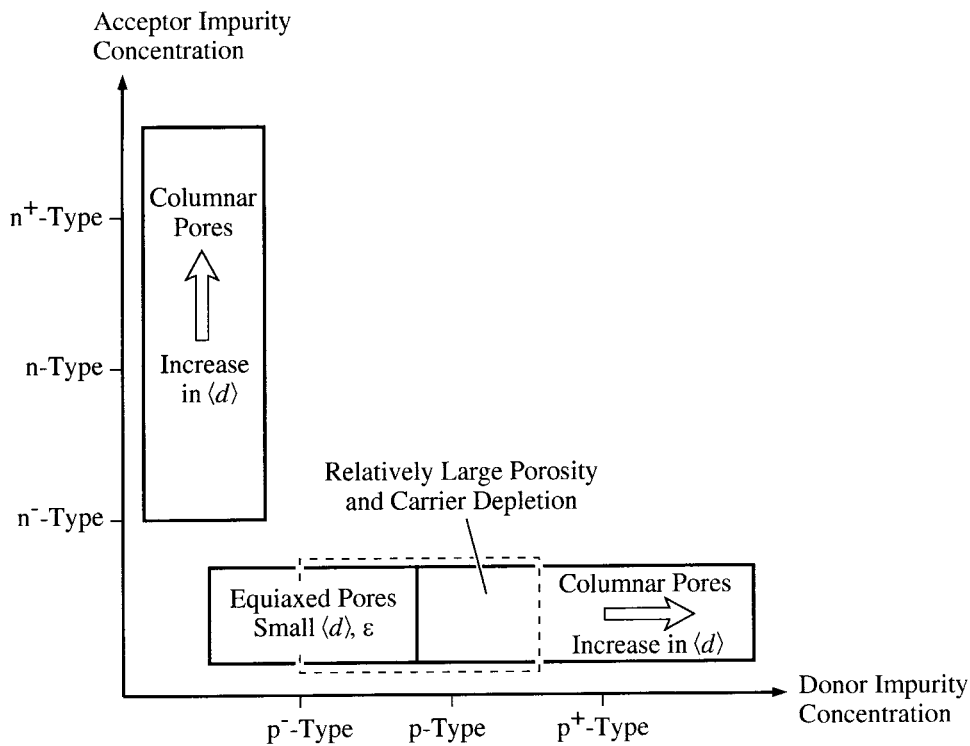


Fig. 3. A classification of the pore morphology, average porosity $\langle \epsilon \rangle$, and average pore size $\langle d \rangle$ for an *n*- and *p*-type porous silicon.

and random network models of porous silicon are shown in Fig. 6(a) and (b). The room temperature thermal conductivity of pure silicon ($k_s = 149$ W/m K)

is used. The doping effect which can be significant at low temperatures [22], is not included. In order to compare the effective thermal conductivity of various porous silicon layers, the average pore size $\langle d \rangle$, the average porosity $\langle \epsilon \rangle$, and the pore morphology, are assumed to be independent of depth δ [13]. Experiments [11] show that the layer thickness does not influence the effective thermal conductivity $\langle k \rangle_{yy}$.

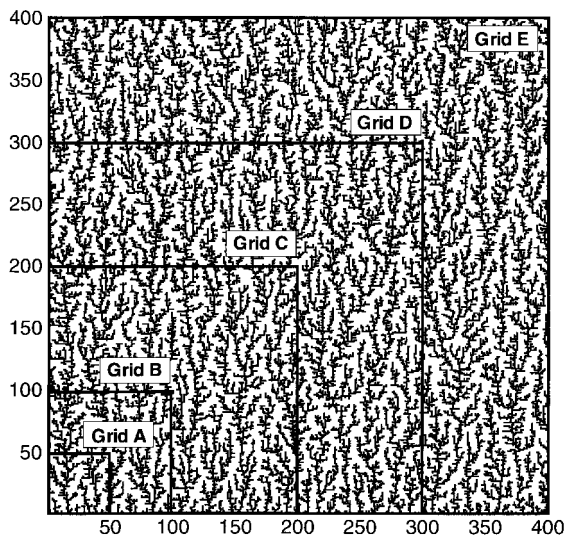


Fig. 4. Pore network and the grid system used. Here the average porosities $\langle \epsilon \rangle = 0.278$ obtained from diffusion-limited simulations by Smith and Collins [34].

3.1. Solution method and verification

Fig. 4 depicts a typical, simulated two-dimensional pore structure for porous silicon. The air-filled pores are shown with shade. The pore structure which is available as a digital data, is used for the grid net. The energy equation (1) is discretized using the finite-volume formulation [23] and then solved using the BASIS solver [24]

When the heat flows across the porous silicon layer, the left and the right control surfaces are taken as adiabatic. The lower and the upper surfaces have prescribed temperatures T_0 and T_δ , respectively. The thermal conductivity jump, across the air–silicon interface, is presented by the harmonic mean of k_f (air, $k_f = 0.0267$ W/m K) and k_s (silicon, $k_s = 149$ W/m K) [23].

The effective thermal conductivity tensor $\langle \mathbf{K} \rangle$, and

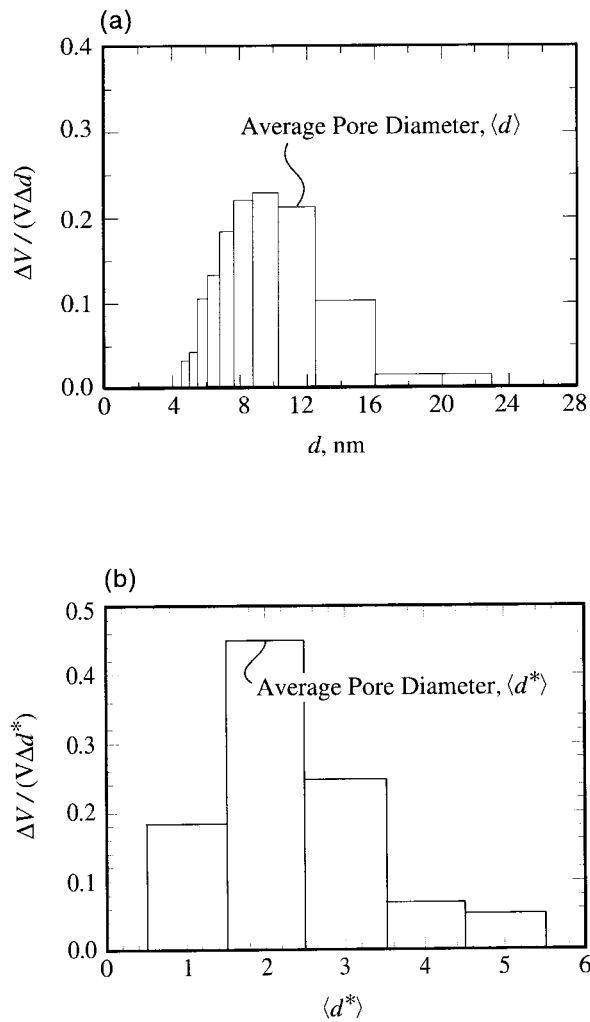


Fig. 5. Typical pore-size distribution for porous silicon: (a) experiment, and (b) from pore structure shown in Fig. 4.

its component across the porous silicon layer $\langle k \rangle_{yy}$, are determined from

$$\langle \mathbf{q} \rangle = -\langle \mathbf{K} \rangle \cdot \nabla T, \quad \langle k \rangle_{yy} = -\frac{\langle q \rangle_{yy}}{(T_0 - T_\delta) / \delta}, \quad (3)$$

where the y -direction heat flux $\langle q \rangle_{yy}$ is found from

$$\langle q \rangle_{yy} = \frac{1}{2L} \left(\int_0^L -k \frac{\partial T}{\partial y} \Big|_{y=0} dx + \int_0^L -k \frac{\partial T}{\partial y} \Big|_{y=\delta} dx \right). \quad (4)$$

The convergence criterion is that the heat fluxes at $y = 0$ and δ be different by less than 0.01%. The lateral effective thermal conductivity $\langle k \rangle_{xx}$ is found similarly.

Validations were made by comparing the computed $\langle k \rangle$ for a cubic array of square inclusions with those reported in Ref. [25]. Complete agreement was found.

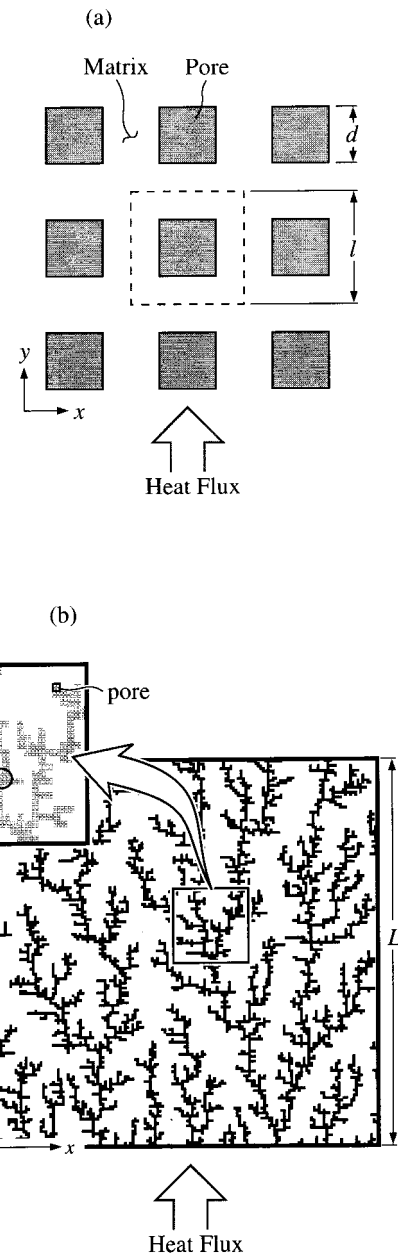


Fig. 6. Schematic diagrams for (a) the two-dimensional unit cell, and (b) the simulated pore-network structure.

3.2. Selection of representative elementary volume

The representative elementary volume was selected by progressively increasing the grid net until the computed volume-averaged porosity $\langle \varepsilon \rangle$ and effective conductivity $\langle k \rangle$ no longer change noticeably. As expected, with the increase in the grid net, the computation time increases substantially. Table 1 and Fig. 7 show the grid size effect on the effective thermal conductivity

Table 1
Grid dependency of the average porosity $\langle \epsilon \rangle$ and the effective thermal conductivity $\langle k \rangle_{yy}$

Grid ($M_x \times M_y$)	$\langle \epsilon \rangle^a$	$\langle k \rangle_{yy}$ (W/m K)
50 × 50 (A)	0.262	28.27
100 × 100 (B)	0.277	18.01
200 × 200 (C)	0.279	17.83
300 × 300 (D)	0.277	16.31
400 × 400 (E)	0.277	16.21

^a The asymptotic average porosity is $\langle \epsilon \rangle_{N \rightarrow \infty} = 0.278$.

and the average porosity for the asymptotic average porosity $\langle \epsilon \rangle = 0.278$. The corresponding grid nets are shown in Fig. 4, for grid nets A to E. As a compromise, the 300 × 300 grid (grid net D) is chosen for this microstructure.

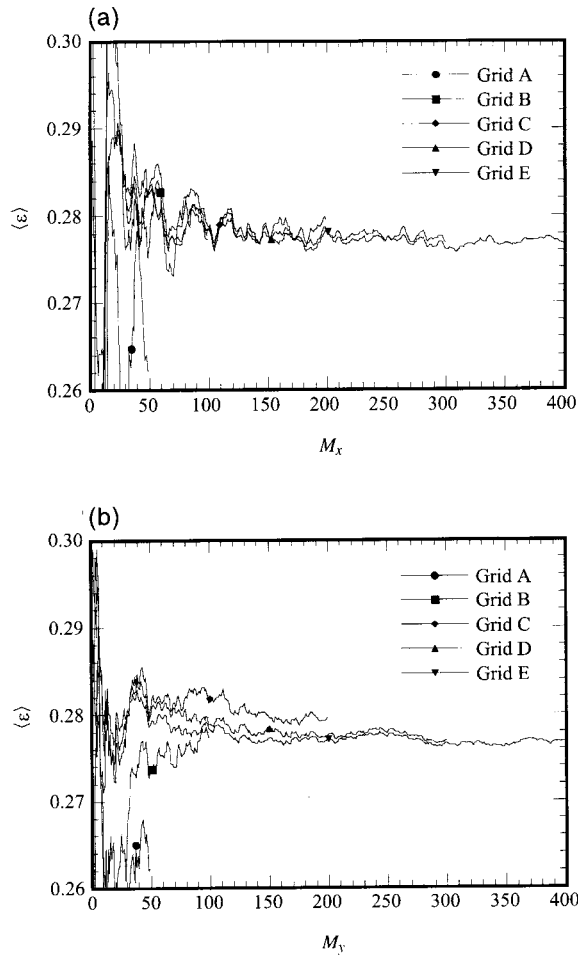


Fig. 7. The variation of average porosity $\langle \epsilon \rangle$ along (a) x -direction, and (b) y -direction and their dependence on grid system of Table 1.

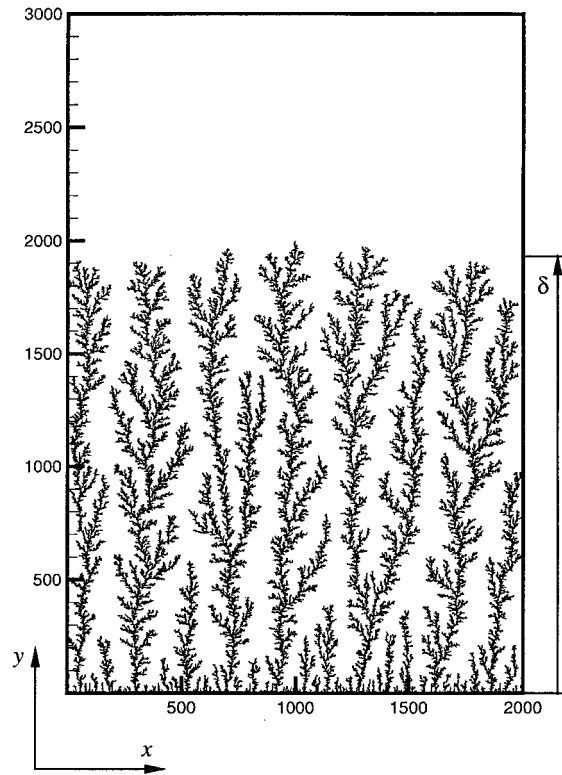


Fig. 8. Typical pore morphology ($\langle \epsilon \rangle = 0.092$) obtained from diffusion-limited simulation by Smith and Collins [34].

For lower porosities, a larger grid net is needed to reach the asymptotic average porosity and effective conductivity. For example, for $\langle \epsilon \rangle = 0.092$ the computed $\langle k \rangle_{yy}$ may not reach the asymptotic value even when the largest available grid (i.e., 2000 × 2000) is used. This structure is shown in Fig. 8. Also, note that for the columnar structures, the structural (and consequently the transport) anisotropy is quite substantial.

4. Boltzmann transport equation

The Boltzmann transport equation is often used to model transport by particles that follow an arbitrary distribution. In a general form, the equation can be written as [8]

$$\frac{\partial f}{\partial t} + u_p \cdot \nabla_r f + \mathbf{a}_p \cdot \nabla_d f = \left(\frac{\partial f}{\partial t} \right)_s \quad (5)$$

Using the analogy between photons and phonons as wave packets of energy, the intensity of phonons I is defined as [26]

$$I = \frac{1}{4\pi} \sum_m \int_0^{\omega_{\max}} |u_{p,m}| f h_P \omega D_m(\omega) d\omega, \quad (6)$$

where D is the density of the states per unit volume, f is the phonon distribution function, h_P is the Planck's constant, $|u_{p,m}|$ is the magnitude of the phonon group velocity, and ω is the phonon frequency. The summation index m is made over the three phonon polarizations. By multiplying Eq. (5) by $|u_{p,m}| h_P \omega D_m(\omega)$ and integrating it over all frequencies, the Boltzmann transport equation can be transformed to the equation of phonon radiative transfer [16], i.e.,

$$\frac{1}{u_p} \frac{\partial I}{\partial t} + \mu \frac{\partial I}{\partial x} + \xi \frac{\partial I}{\partial y} = \frac{I^0(T(x)) - I}{u_p \tau(T)}, \quad (7)$$

where μ and ξ are the directional cosines. It is evident that this equation is similar to the photon equation of radiative transfer [27]

$$\begin{aligned} \frac{1}{c} \frac{\partial I}{\partial t} + \mu \frac{\partial I}{\partial x} + \xi \frac{\partial I}{\partial y} &= \sigma_a I_b - \sigma_{\text{ex}} I \\ &+ \frac{\sigma_s}{4\pi} \int_{4\pi} I(r, \hat{s}') \Phi(r, \hat{s}', \hat{s}) d\Phi', \end{aligned} \quad (8)$$

where c is the speed of light, σ_a , σ_{ex} , and σ_s are absorption, extinction, and scattering coefficients, and Φ is the phase function. This similarity gives an easy access to the solution methods which are well developed for the equation of radiative transfer.

For steady state, the two equations (7) and (8) are exactly the same if scattering is neglected (i.e., $\sigma_s = 0$). This does not mean that Eq. (7) can deal with only non-scattering media. As will be shown later, the main reduction of the heat flow rate is due to the scattering mechanism such as defects, dislocations, boundaries and particle interactions. So the inclusion of scattering effects is important in phonon transport. The various scatterings are modelled using relaxation time τ , in Eq. (7). In Eq. (7), several bulk material properties are prescribed, these include the specific heat, the phonon group velocity, and the phonon mean-free path (or relaxation time).

Once the intensity is found by solving Eq. (7), the radiative heat flux can be determined from

$$q(r) = \int_{\Phi=4\pi} \mu I(r, \Phi) d\Phi. \quad (9)$$

4.1. Solution method and verification

The discrete ordinate method (S_N method) is a tool to transform the equation of radiative transfer into a set of simultaneous partial differential equations. This is based on a discrete representation of the directional variation of the radiative intensity I . A solution to the

transport problem is found by solving the equation of radiative transfer for a set of discrete directions spanning the entire solid angle. The integrals over the solid angle are approximated by numerical quadrature. This method is widely accepted and a comprehensive discussion is available [28].

For a specific ordinate direction m , defined by $\Phi_m = (\mu_m, \xi_m)$, Eq. (7) can be approximated as

$$\begin{aligned} \left[\mu_m \frac{\partial}{\partial x} + \xi_m \frac{\partial}{\partial y} + \sigma_a(x, y) \right] I_m(x, y) \\ = \sigma_a(x, y) I_b(x, y). \end{aligned} \quad (10)$$

To solve the discrete ordinate equation, the rectangular enclosure is subdivided into small control volumes in a $M_x \times M_y$ net. Within each control volume, the spatially discretized equation for the radiative intensity in the ordinate direction Φ_m is derived as

$$\begin{aligned} [\mu_m (A_e I_{em} - A_w I_{wm}) \\ + \xi_m (B_n I_{nm} - B_s I_{sm})] + \Delta V I_{pm} = \Delta V S_{pm} \end{aligned} \quad (11)$$

for $m = 1, \dots, M$,

where e, w, n, s are the boundaries in the compass directions and p is the center point of the control volume. The area and volume elements assume a unit depth in the z direction.

The number of unknown I s in Eq. (11) are reduced by using one of several relationships between the control-volume boundary intensities and the center point intensity. The weighted diamond difference scheme is used in this study to relate the intensities in the control volume. The weighted relationship of the cell boundary intensities to the average intensity in the cell is expressed as

$$\begin{aligned} I_{pm} &= w_{xm} I_{em} + (1 - w_{xm}) I_{wm} \\ &= w_{ym} I_{nm} + (1 - w_{ym}) I_{sm}. \end{aligned} \quad (12)$$

To avoid negative intensities, a scheme suggested by Lathrop [29] is applied in selecting the differencing weights.

If I_{wm} and I_{sm} are assumed to be known, where the iteration is in the direction with a positive directional cosines and in increasing space dimensions, then Eq. (11) can be reduced to eliminate the intensities I_{em} and I_{nm} , using Eq. (12). Solving for I_{pm} yields

$$\begin{aligned} I_{pm} = \frac{\mu_m A I_{wm} + \xi_m B I_{sm} + \Delta V S_{pm}}{\mu_m A_e / w_{xm} + \xi_m B_n / w_{ym} + \Delta V}, \end{aligned} \quad (13)$$

for $\mu_m, \xi_m > 0$,

where

$$A = (1 - w_{xm})A_e/w_{xm} + A_w$$

$$B = (1 - w_{ym})B_n/w_{ym} + B_s. \tag{14}$$

Special attention is needed for the selection of the ordinates set, μ_m and ξ_m . To satisfy the continuity at the interface, the set of ordinates and weights should also satisfy the first moment over a half range, that is,

$$\int_{\hat{n}\cdot\hat{s}<0} |\hat{n}\cdot\hat{s}| d\Phi = \int_{\hat{n}\cdot\hat{s}>0} \hat{n}\cdot\hat{s} d\Phi = \pi = \sum_{\hat{n}\cdot\hat{s}>0} w_j \hat{n}\cdot\hat{s}_j. \tag{15}$$

The set of ordinates and weights satisfying Eq. (15) is taken from Fiveland [30].

Once all directional intensities for each finite volume have been calculated, the values for the boundary and source terms may be updated, and the procedure is repeated until the convergence criteria are met. Convergence is checked during the iteration process using the cell-average intensities at the current and the previous iterations. It is assumed that the convergence is obtained when the maximum percentage error of the intensities is less than 0.0001%.

In the limit where the domain length scale is large compared to phonon mean-free path, the Fourier law should be recovered. In this optically thick case, the diffusion approximation is valid. Considering the jump boundary condition, Deissler suggested the following solution [31]

$$q = \frac{\sigma_{SB}(T_1^4 - T_2^4)}{\frac{3}{4}\left(\frac{L}{\lambda}\right) + 1} \approx \frac{4\sigma_{SB}T^3\Delta T}{\frac{3}{4}\left(\frac{L}{\lambda}\right) + 1}. \tag{16}$$

Comparing Eq. (16) with Eqs. (1) and (2), the Stefan–Boltzmann constant σ_{SB} for phonon can be obtained as

$$\sigma_{SB} = \frac{\rho c_p u_p}{16T^3}. \tag{17}$$

As a validation, as shown in Fig. 9, the predicted thermal conductivity of silicon approaches as asymptotic behavior (Fourier behavior) as the domain size increases.

For a further validation, the thermal conductivity of silicon layer is compared with the experiment by Ashghi et al. [32]. Good agreement is found in the experimental error range. Also, the predicted results for the one-dimensional, multi-layer composites are compared with the available results [18]. The boundary and interface between layers are shown in Fig. 10(a). Complete agreement is found, as shown in Fig. 10(b). The room-temperature properties used in the computation of thermal conductivity of GaAs/AlAs and Si/

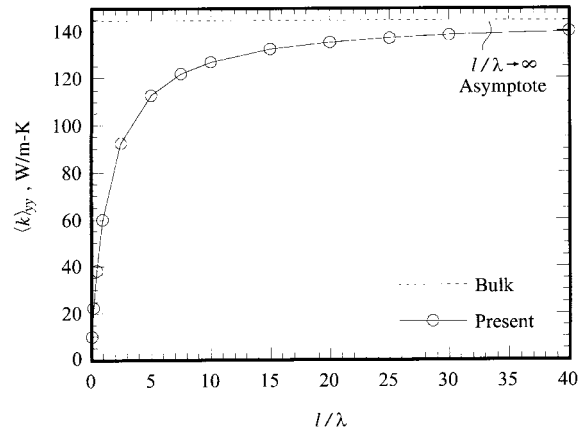


Fig. 9. Predicted asymptotic behavior of thermal conductivity with respect to acoustical thickness.

Ge layer composites are given in Table 2. Note that the lattice mismatch between Si/Ge layer composite is much larger than that of GaAs/AlAs, but the agreements are still fair. This agreement gives confidence to the analysis of porous silicon, where phonons are almost totally reflected from silicon–air interface.

4.2. Boundary and pore interface conditions

The treatment of boundaries and pore interface in the two-dimensional, unit-cell model (Fig. 6(a)) and the network model (Fig. 6(b)) is similar to that for the one-dimensional, multi-layer composites.

Ziman [8] proposed the following expression for estimating the interface scattering parameter p :

$$p \approx \exp\left(-16\pi^3 \delta_r^2 / \lambda^2\right), \tag{18}$$

where λ is the carrier wavelength and δ_r is the mean interface roughness. At room temperature, the dominant phonon wavelength is $\lambda \sim 10\text{--}20 \text{ \AA}$. Then, even for a monolayer the roughness is $\delta_r \sim 3 \text{ \AA}$. This gives an interface scattering parameter of nearly zero, and allows for the assumption of a totally diffuse interface.

The interface between layers reflects and transmits

Table 2
Room-temperature properties used in the computation of the thermal conductivity of GaAs/AlAs and Si/Ge superlattices

Material	$\rho c_p \times 10^6$ (J/m ³ K)	u_p (m/s)	λ_p (Å)
GaAs	1.71	3700	208
AlAs	1.58	4430	377
Si	1.66	6400	409
Ge	1.67	3900	275

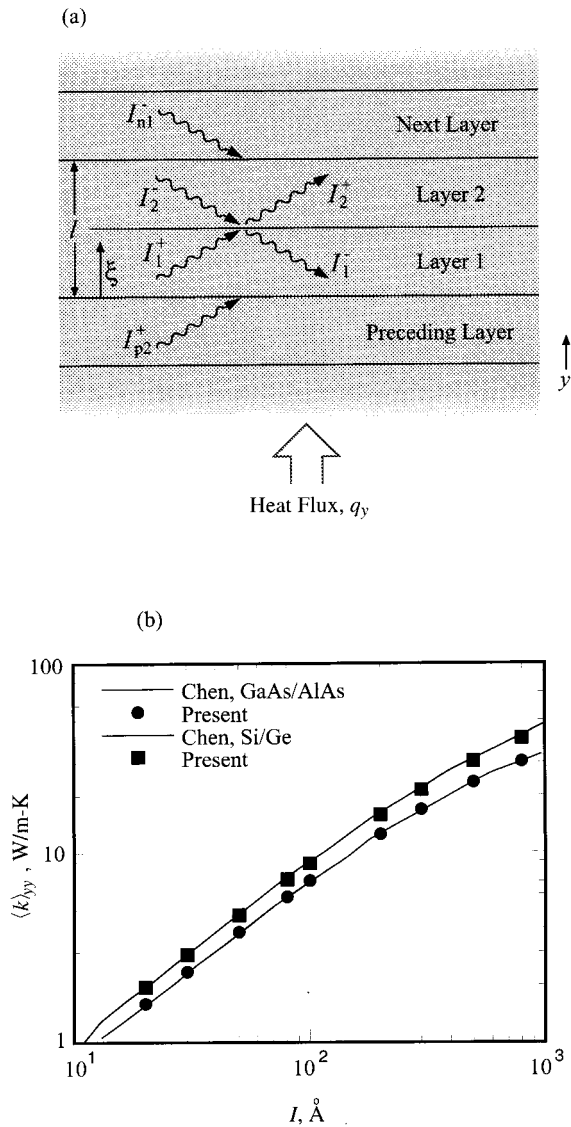


Fig. 10. Comparison of the predicted thickness dependence of thermal conductivity, in multi-layer composites (a) with the available predictions (b).

phonons and adds to the resistance to the heat flow. Referring to Fig. 10(a) for a totally diffuse interface, the energy balance at bottom surface gives

$$I_1^+(\xi=0) = \frac{R_{d12}}{\pi} \int \Phi' I_1^-(\xi=0) d\Phi' + \frac{T_{d21}}{\pi} \int \Phi' I_{p2}^+(\xi=0) d\Phi', \quad (19)$$

where I_{p2}^+ is the phonon intensity at $\xi=0$ in the layer preceding layer 1. Using periodic conditions, I_{p2}^+ is expressed as [18]

$$I_{p2}^+ = I_2^+ + \frac{u_{p,2} \rho c_{p,2} (T_0 - T_L)}{4\pi}. \quad (20)$$

Similarly, the energy balance at the internal interface and the top surface, forming one period of the multi-layer composite, gives

$$I_1^-(\xi=\xi_i) = \frac{R_{d12}}{\pi} \int \Phi' I_1^+(\xi=\xi_i) d\Phi' + \frac{T_{d21}}{\pi} \int \Phi' I_2^-(\xi=\xi_i) d\Phi', \quad (21)$$

$$I_2^+(\xi=\xi_i) = \frac{R_{d21}}{\pi} \int \Phi' I_2^-(\xi=\xi_i) d\Phi' + \frac{T_{d12}}{\pi} \int \Phi' I_1^+(\xi=\xi_i) d\Phi', \quad (22)$$

$$I_2^-(\xi=\xi_L) = \frac{R_{d21}}{\pi} \int \Phi' I_2^+(\xi=\xi_L) d\Phi' + \frac{T_{d12}}{\pi} \int \Phi' I_{n1}^-(\xi=\xi_L) d\Phi', \quad (23)$$

where the integration with respect to the solid angle is over the half space and R_{dij} and T_{dij} are the reflectivity and transmissivity at an interface for phonons incident from the i layer towards the j layer.

The relation between the reflectivity and transmissivity, and the transmissivity at the totally diffuse scattering limit, are obtained based on the diffuse scattering limit model of Swartz and Pohl [33], i.e.,

$$T_{dji} = R_{dij} = 1 - T_{dij} \quad (24)$$

$$T_{dij} = \frac{\rho c_{p,j} u_{p,j}}{\rho c_{p,i} u_{p,i} + \rho c_{p,j} u_{p,j}}. \quad (25)$$

4.3. Unit-cell model

The unit cell described in Fig. 6(a) is a starting point for modeling the effective thermal conductivity of a porous medium. When the porous medium has a periodic structure, successful predictions have been made [2–4]. These are based on the Fourier treatment and the effect of the unit cell (or pore) size has not yet been addressed. On the other hand, the existing treatments based on Boltzmann transport equation are for one-dimensional layers, although it gives elegant semi-analytic solution. Considering the practical applications such as the porous silicon, the two-dimensional extension of the Boltzmann approach is needed.

Here we have considered three pore sizes ($d = 1, 3, 5$ nm). Given the pore sizes, the unit cell linear dimension l is determined using the porosity defined as

Table 3
The effect of grid size on the effective conductivity $\langle k \rangle_{yy}$ for the S_4 quadrature set for $\langle \varepsilon \rangle = 0.201$

Grid	$\langle k \rangle_{yy}$ (W/m K)	
	$d = 1$ nm	$d = 3$ nm
67×67	8.8659	21.4229
87×87	6.0112	15.1683
131×131	5.5386	13.9619
159×159	6.3194	15.6150
203×203	4.8340	11.9502
251×251	4.2461	10.3032
315×315	3.3201	8.3454

$\varepsilon = d^2/l^2$. The effective thermal conductivity is then determined from

$$\langle k_{yy} \rangle = - \frac{\langle q \rangle_{yy}}{(T_0 - T_l)/l} \quad (26)$$

where the y -direction radiation heat flux $\langle q \rangle_{yy}$ is

$$\langle q \rangle_{yy} = \frac{1}{2l} \left\{ \int_0^l q_{yy}(x, 0) dx + \int_0^l q_{yy}(x, l) dx \right\}. \quad (27)$$

The radiation heat flux, q_{yy} is defined in Eq. (9). The convergence criterion requires that the first and second terms be very close (i.e., much less than 1% for small network grid and as large as a few percent for the largest grid).

4.4. Selection of representative elementary volume

For the random pore network model, the representative elementary volume is similar to that of Section 3.2. Table 3 lists the grid systems tested for the pore network with the asymptotic average porosity of $\langle \varepsilon \rangle = 0.201$. The corresponding selected pore distribution is shown in Fig. 11 for grids A to G. For computational economy, the 315×315 grid (grid G) is selected for this porosity. Note that every grid point in Fig. 4 corresponds to four subgrids (two in x -direction and two in y -direction) in Fig. 11, since additional subgrids are needed to handle the pore interface. Fig. 7(a) and (b) show the porosity convergence for this grid set.

Table 4 shows the effect of the discrete ordinate quadrature sets for a 67×67 grid net, $d = 1$ nm and $\langle \varepsilon \rangle = 0.201$, on the predicted effective conductivity. The S_4 approximation, which computes 12 fluxes over the hemisphere, is used for all of cases considered.

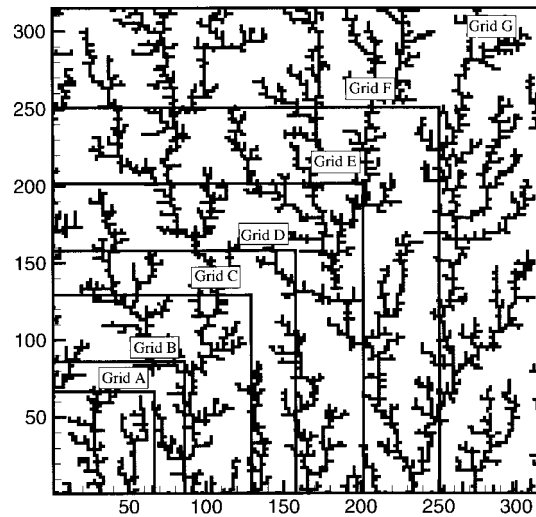


Fig. 11. The grid system used and the typical pore morphology ($\langle \varepsilon \rangle = 0.201$).

5. Results and discussion

To show the effect of pore-network randomness, we use the Fourier treatment of Section 3 and to show the effect of pore size, we use the Boltzmann treatment of Section 4. Gesele et al. [11] suggest a simple relation for the combined effects of the morphology and the size. They suggest that Eq. (2) be modified as

$$\langle k \rangle = \frac{1}{3} (1 - \langle \varepsilon \rangle)^3 \rho c_p u_p l, \quad (28)$$

where they suggest that the pore-network randomness effect be modeled with $(1 - \langle \varepsilon \rangle)^3$ and the pore-size effect with l . However, this does not correctly predict the experiments for low porosity and does not satisfy the $\langle \varepsilon \rangle \rightarrow 0$ asymptote, unless l is continuously changed with $l \rightarrow \lambda_p$ for $\langle \varepsilon \rangle \rightarrow 0$.

To explain the effect of pore-network randomness and the pore size on $\langle \mathbf{K} \rangle$, four different computations are made, namely, (1) Fourier treatment plus unit cell, (2) Fourier treatment plus network, (3) Boltzmann

Table 4
The effect of the discrete ordinate quadrature sets (67×67 grid, $d = 1$ nm), $\langle \varepsilon \rangle = 0.201$ on the effective conductivity $\langle k \rangle_{yy}$

	$\langle k \rangle_{yy}$ (W/m K)
S_4	8.8659
S_6	8.9223
S_8	8.6231
S_{10}	9.0529

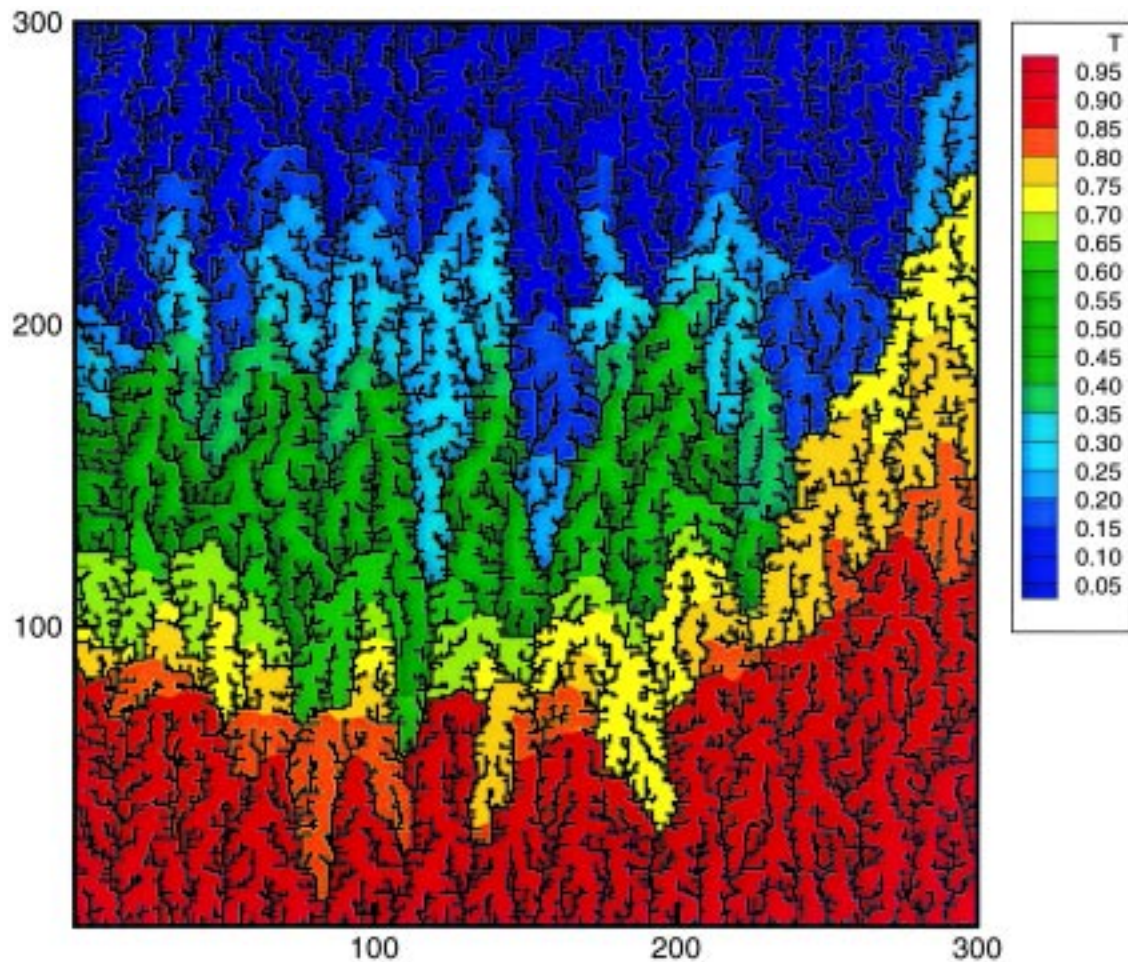


Fig. 12. The pore-network structure and predicted temperature distribution for grid D in Fig. 4. The heat flows across the porous layer.

treatment plus unit cell, and (4) Boltzmann treatment plus network.

5.1. Effect of pore-network randomness

To demonstrate the effect of pore-network randomness, $\langle k \rangle_{yy}$ is determined based on the Fourier treatment using the simulated pore-network model. The pore structure and the distribution of the normalized temperature $(T - T_\delta)/(T_0 - T_\delta)$, for grid D in Fig. 4, are shown together in Fig. 12. The air-filled pores are shown with shade. Fig. 12 shows how the high conductivity solid fingers the heat into the layer, while the low conductivity air causes a large temperature drop. The isothermal lines follow the high-conductivity solid-phase distribution. Also note that the random pore structure requires a large representative elementary volume for achieving an asymptotic (grid-size independent) behavior.

For a variety of applications, high porosity (e.g., $\langle \epsilon \rangle > 0.4$) porous silicon is more desirable and most experiments have been conducted for this range. However, the simulation of Smith and Collins [34] are for relatively low porosities (i.e., $\langle \epsilon \rangle < 0.28$). For comparison with the experiments, the low-porosity simulations can be slightly extrapolated. Two additional pore networks with slightly larger porosities ($\langle \epsilon \rangle = 0.322$ and 0.380) are formed using the available network for the largest porosity ($\langle \epsilon \rangle = 0.278$). Different enlargement factors are applied to the solid phase and the pore volume. Then the enlarged domain size is scaled to its initial value. For validation of this process, a pore network with $\langle \epsilon \rangle = 0.252$, is produced using the available pore network with $\langle \epsilon \rangle = 0.208$. It is found that the predicted effective thermal conductivities are in good agreement.

The uncertainty associated with extensive extrapolations is partly due to the highly irregular pore struc-

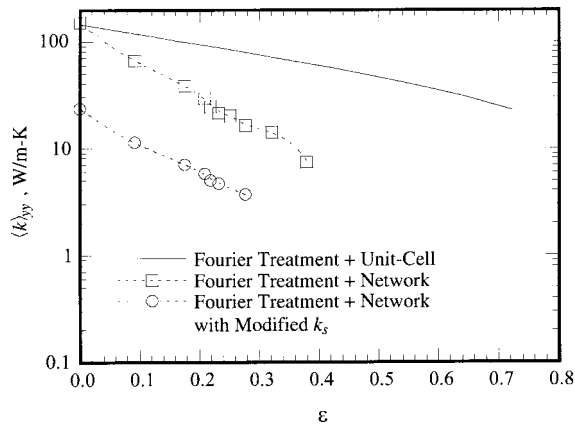


Fig. 13. The effect of pore-network randomness on effective conductivity is shown by comparing the predicted effective thermal conductivity using the Fourier treatment plus network with the Fourier treatment plus unit cell.

ture and partly due to lack of availability of a large set of simulated networks.

Fig. 13 shows the predicted variation of the effective thermal conductivity $\langle k \rangle_{yy}$ with respect to porosity. By noting the difference with the results of the unit-cell model, we note that the heat transfer is significantly hindered by the pore-network randomness.

5.2. Effect of phonon pore scattering

The mean-free path can be determined using Eq. (2). At room temperature bulk thermal conductivity of silicon is $k_s = 149$ W/m K, and its volumetric heat capacity is $\rho c_p = 1.659 \times 10^6$ J/m³ K [35]. A special average of the transverse and the longitudinal phonon velocities, $u_p^{-1} = \frac{1}{3}(2u_{p,T}^{-1} + u_{p,L}^{-1})^{-1} = 6.53 \times 10^3$ m/s, is used [36]. This gives the bulk phonon mean-free path $\lambda_{p,0} \sim 40$ nm. According to Flick et al. [37], the size effects on heat conduction becomes important when $\langle l \rangle < 7\lambda_{p,0} \simeq 280$ nm and this is larger than the average pore size $\langle d \rangle$ for porous silicon considered here. The small pore wall thickness introduces an additional resistance to heat flow.

To apply the Boltzmann transport equation, the wall-pore dimension should be larger than the phonon wavelength. At room temperature, the phonon wavelength for silicon is approximately $a\theta_D/T \simeq 1.1$ nm [17]. Also, the quantum size effect is negligible in this large length scale. We also note that as the linear dimension of the representative elementary volume increases, the optical thickness increases. Also, when the transmission through the network is very small, numerical difficulties are encountered [38]. The average pore size for porous silicon can be controlled over three orders of magnitude from order of 1–100 nm.

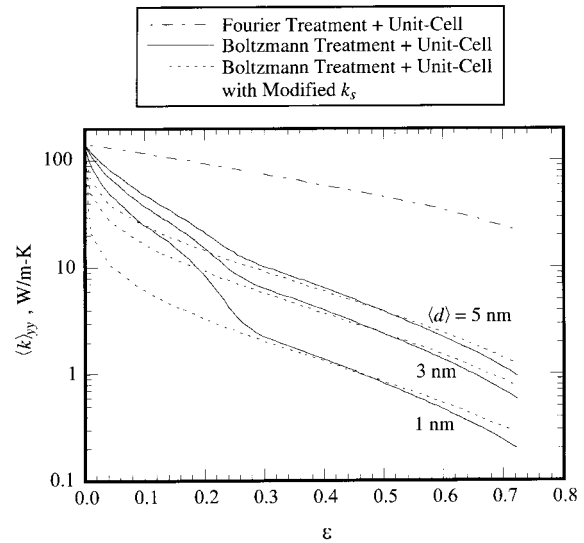


Fig. 14. The effect of phonon pore scattering on the effective conductivity is shown by comparing the predicted effective thermal conductivity using the Fourier treatment plus unit cell with the Boltzmann treatment plus unit cell.

Based on the experimental results and to demonstrate the size effect, three pore sizes ($\langle d \rangle = 1, 3$ and 5 nm) are used.

Fig. 14 shows the predicted effective thermal conductivity, defined in Eq. (26), for the unit-cell model using the Fourier and Boltzmann treatments. Since the effective phonon mean-free path λ_p is limited by the pore boundary scattering, the reduction of effective thermal conductivity is apparent as the pore size $\langle d \rangle$ is decreased. Abrupt changes near $\epsilon = 0.2$ is found. This occurs as the ratio of pore size to the unit cell size reaches a threshold value where a significant amount of the phonon energy is reflected at the pore boundary. Note that the pore boundary scattering is dominant here, because of the long bulk mean-free path $\lambda_{p,0}$ compared to the unit cell size $\langle l \rangle$.

Fig. 15 shows the temperature distributions obtained from Boltzmann treatment (Fig. 15(a)–(e)) with respect to pore size d . The pore size varies between $d = 1$ –500 nm. The asymptotic temperature distribution ($d \rightarrow \infty$) obtained from the Fourier treatment is also shown (Fig. 15(f)). The results are for $\epsilon = 0.16$. The agreement between the two treatments, for large d , is clear in Fig. 15. From the Boltzmann treatment with a small pore size, a temperature jump is found at the interface. This is similar to that for the one-dimensional, multi-layer composite. Due to the total reflection at the pore boundary, some localized hot and cold regions are found below and above the pore.

To account for the size effect, Majumdar [16] suggests a size-affected, mean-free path, given by

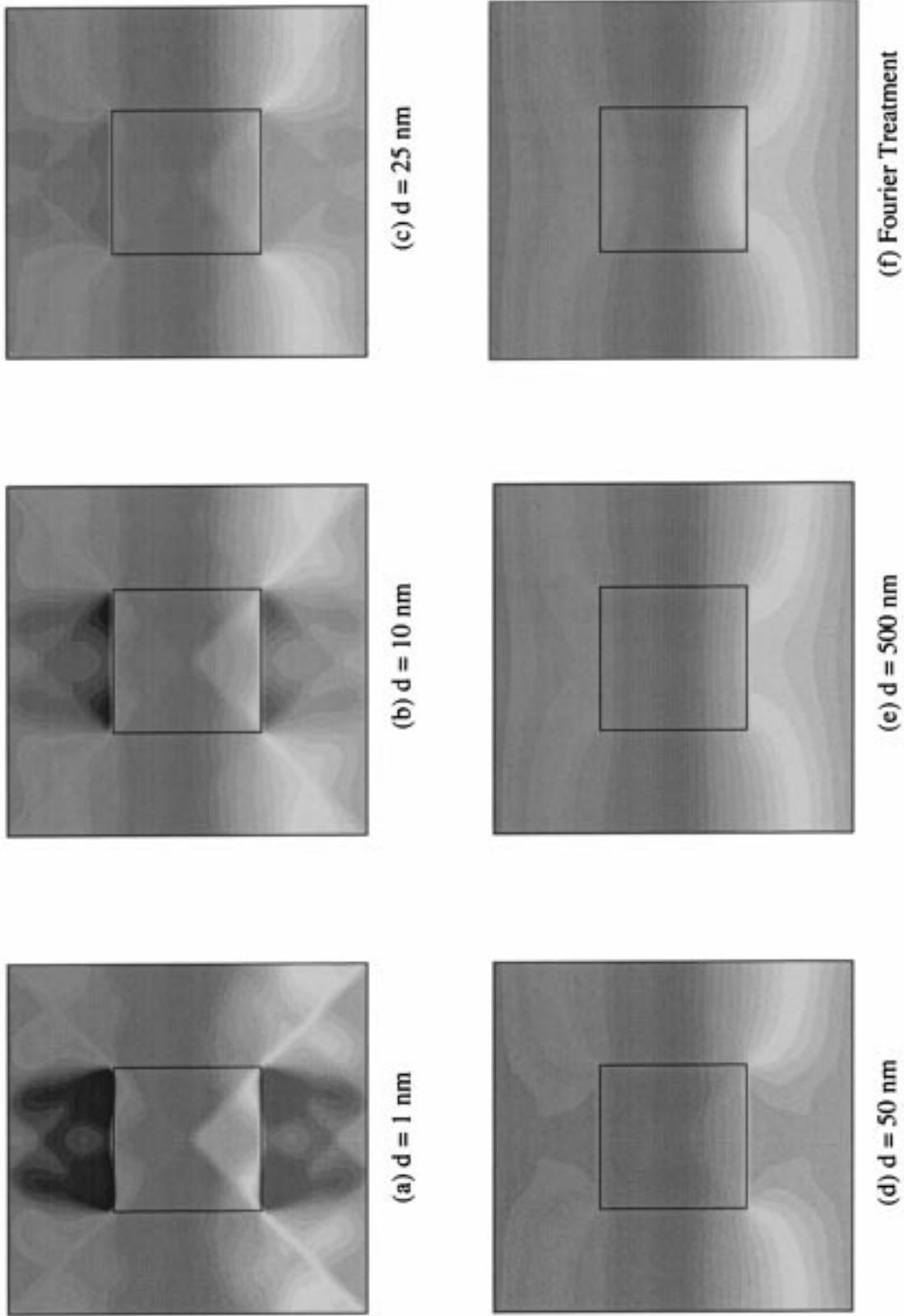


Fig. 15. The temperature distributions obtained from the Boltzmann treatment for (a) $d = 1$, (b) 10, (c) 25, (d) 50, and (e) 500 nm. The asymptotic temperature distribution ($t \rightarrow \infty$) obtained from the Fourier treatment is also shown (f).

$$\lambda_p = \frac{\lambda_{p,0}}{1 + \frac{4}{3} \frac{\lambda_{p,0}}{l'}} \tag{29}$$

which may be used to determine k_s in Eq. (2). For a one-dimensional layer, the characteristic length l' is the layer thickness. But, for a two-dimensional unit cell, we use an equivalent length defined as $l'^2 = l^2 - d^2$. This is an equivalent length after the pore is removed from the unit cell. Using this modified k_s in the Fourier treatment of unit-cell model, the predicted effective conductivities are shown in Fig. 14. The good agreement with the results of the Boltzmann treatment at the higher porosity is noted, although the asymptotic behavior at low porosity is not in agreement. Also shown in Fig. 13 is the result using the Eq. (29) with $d = 10$ nm. This gives $\lambda_p = 0.158\lambda_{p,0}$, which gives a solid conductivity $k_s = 23.5$ W/m K. This characteristic length represents experimental samples A, B and a in Fig. 17.

5.3. Lateral effective conductivity

Due to the anisotropic pore morphology, the effective conductivity is not isotropic and a preferential conduction occurs along the y direction, shown in Fig. 1. The predicted variation of the lateral effective conductivity $\langle k \rangle_{xx}$ with respect to porosity is shown in Fig. 16. Here the ratio $\langle k \rangle_{xx} / \langle k \rangle_{yy}$ is also used to emphasize the anisotropy. There are no available experimental data for comparison. The overall trend in the porosity dependency is similar to that of $\langle k \rangle_{yy}$. The pore branches completely break the solid-phase connectivity and the resulting serial arrangement of phases leads to a very low thermal conductivity. This is not

expected in three-dimensional structures, where the solid-phase continuity results in higher effective conductivity.

6. Comparison with experiments

The available experimental results are too few and not consistent. They also lack sufficient geometrical information for a direct comparison with the predictions. Drost et al. [9] used a dynamic conductivity measurement technique based on the thermal waves traveling in the specimen. However, as mentioned by Benedetto et al. [10], the measurement technique by Drost et al. is rather complicated and cannot be used for different sample types. Also, the undesirable effect of SiC layers, which are needed to cover the porous silicon, in the dynamic conductivity measurement, should be removed. Benedetto et al. [10] measured $\langle k \rangle_{yy}$ for porous-silicon layers using a photoacoustic technique and Gesele et al. [11] used the $3-\omega$ technique. The measurements are summarized in Table 5. Among the parameters, the porosity, the morphology, and the pore size are used in the prediction. The pore sizes reported by Drost et al., and Gesele et al., are well documented. However, the pore sizes in the experiment of Benedetto et al., are not given and are assumed to be similar to those in experiments of Beale et al. [13].

The experimental results for $\langle k \rangle_{yy}$ are shown along with the various predictions in Fig. 17. Samples A, B, II, III, and 'a' have similar pore structure as shown in Fig. 4, which is a highly-branched, columnar structure. Sample III shows a large difference between the oxidized and the fresh samples and the high values are

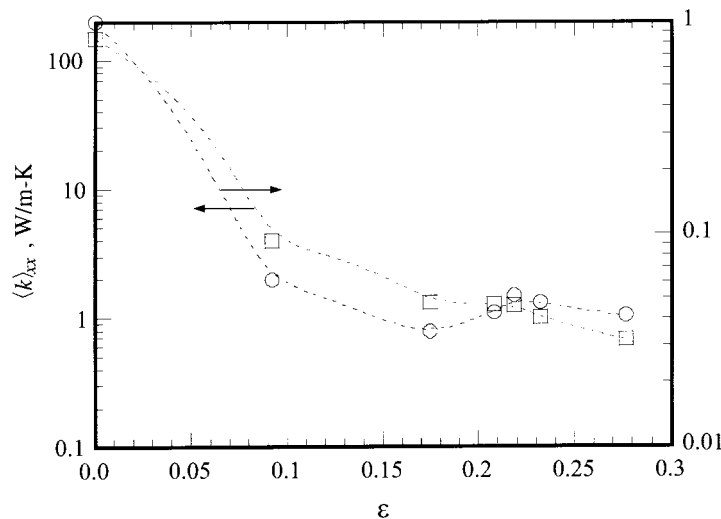


Fig. 16. The predicted variation of the lateral effective thermal conductivity $\langle k \rangle_{xx}$ with respect to porosity ϵ .

Table 5
The doping and etching parameters, and experimental results for various porous silicon samples

Sample ^a	A	B	C	D	I	II	III	a	b	c	d	e
Resistivity, ρ_e (Ω cm)	0.01	0.01	10	10	38.0–52.0	1–2	0.010–0.018	0.01			0.02	
HF concentration (%)	20	12	12	12	–	–	–	–		48		
Current density (mA/cm ²)	15	15	86	86	30	10	50	–		–		
Etching time (s)	1800	1800	720	3000	420	900	240	–		–		
Illumination applied	–	–	None	None	None	Halogen	None	–		–		
Porosity, ϵ	0.60	0.50	0.40	0.40	0.40	0.53	0.45	0.64	0.64	0.71	0.79	0.89
Layer thickness, δ (μ m)	23	10	75	175	10	10	10	21	31	31	31	35
Silicon wafer type	p^+	p^+	n^-	n^-	p^-	n^-	p^+	p^+			p^-	
Morphology			Columnar		Equiaxed		Columnar				Equiaxed	
Pore size, d (nm)	> 12	~12	–	~500/~200	~3	≥ 100	~100	9.0 \pm 3.0	1.7 \pm 0.5	2.0 \pm 0.3	2.7 \pm 0.3	4.5 \pm 0.6
$\langle k \rangle_{yy}$ (W/m K)	2.5	3.9	31.2	10.4/31.2 ^b	1.2/1.3 ^c	1.75/1.85	80/2.7	0.79	0.196	0.135	0.058	0.035

^a A–D: Benedetto et al. [10]; I–III: Drost et al. [9]; a–e: Gessele et al. [11].

^b Two layers. One layer of $\langle k \rangle_{yy} = 10.4$ with pore diameter 500 nm and the other of $\langle k \rangle_{yy} = 31.2$ with pore diameter 200 nm.

^c The upper parts are for specimen as prepared and the lower parts are for oxidized specimen.

not in line with the other experimental results. Note that the n -type silicon sample with the light illumination (II), is very similar to the p -type silicon samples (A, B, III and a). The important difference is in its large pore size ($\langle d \rangle \sim 100$ nm) compared to the p -type samples ($\langle d \rangle \sim 10$ nm for A, B, and a). Sample C is also n -type, but light illumination is not applied. Smith and Collins [14] report that the pore-like straight cylindrical channels are produced for this sample. Thus for sample C, the heat flow is not as much prohibited as the highly branched structures. This explains the large effective thermal conductivity of sample C. The results for sample III without oxidation is questionable, because the measured thermal conductivity is almost near the value for the parallel arrangement of phases which is the theoretical upper limit.

Samples I and b–e also have similar pore structures, i.e., equiaxed. Thus, their thermal conductivity follows the same trend, but is lower than that of columnar structures.

Also shown in Fig. 17 are the various predictions. These are Fourier treatments with the network model and Boltzmann treatment with the same structure models. The network models are limited to $\langle \epsilon \rangle < 0.4$. Starting with the Boltzmann treatment with the unit-cell model, we note that the effective thermal conductivity for pore sizes $\langle d \rangle = 1$ and 3 nm are lower than the experiments A and B. Since the thermal conductivity reduction is due to a combined effect of the pore randomness and the pore size, the result of unit-cell model, which includes only the size effect, should not exceed the experimental results. There are several explanations for this. The most obvious one is the uncertainty in the estimation of the pore size. As the pore size increases (i.e., $\langle d \rangle = 5$ nm), the predicted effective thermal conductivity becomes larger than the experiments. Note that the pore size definition used in the experiments is different from that used in the simulations. As shown in Fig. 6(b), the pore size in the simulation is the grid size (as compared to the actual pore size in experiments A, B, and C as shown in Fig. 6(b)). Then we expect the simulated pore sizes to be smaller than the experiments. Currently there is no clear correspondence between these two. The two-dimensional limitation is another reason for this difference. The three-dimensional effective thermal conductivity is expected to be larger [7].

Using the random pore network, the predicted effective thermal conductivity using the Fourier treatment is shown in Fig. 17. As is evident, the predicted effective thermal conductivity is larger than the experiments and this may be due to the size effect (pore scattering).

The combined effect of the pore-network randomness and pore size is shown through the Boltzmann treatment plus the random network model in Fig. 17. Although only three different porosities

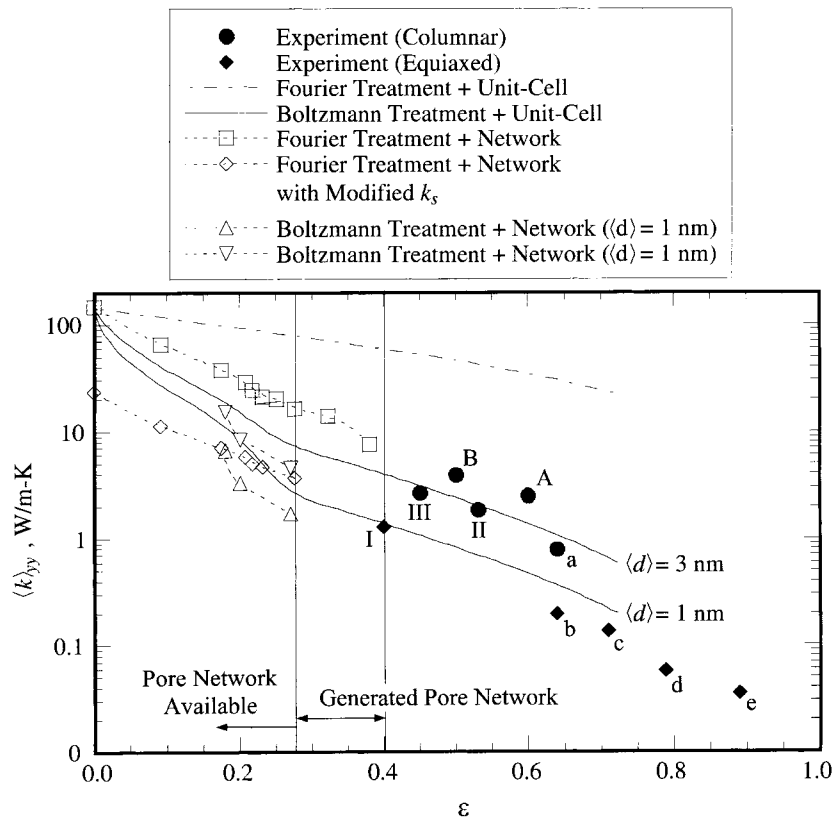


Fig. 17. Comparison of the predicted effective thermal conductivity of porous silicon $\langle k \rangle_{yy}$, with the available experiments.

($\epsilon = 0.177, 0.201$ and 0.271) and two different pore sizes ($\langle d \rangle = 1$ and 3 nm) are simulated, the significant reduction in the heat flow rate by pore randomness and pore scattering, is apparent.

7. Conclusions

Direct simulation of conduction through anisotropic porous silicon layers is made, using two-dimensional matrix structures along with the Boltzmann transport equation. The observed low conductivity, i.e., lower effective phonon mean-free path, can be explained with the inclusion of the effects of the phonon pore scattering and the pore randomness. The hindering effect of the phonon pore scattering (due to the reflection from at the solid-pore interface) is significant. Also, due to the dendritic structure of the pores, the hindering effect of the pore-network randomness is also significant. The predictions are compared with the existing experiments and considering the lack of structural data in the experiments, a good agreement is found.

Acknowledgements

The authors are thankful to Professor Collins for the digital data from his simulations. We would also like to thank Dr. Amir A.M. Oliveira for his assistance with the pore-size distribution for porous silicon. The financial support of the National Science Foundation through grant CST-97-14157, is greatly appreciated. The first author (J.D. Chung) would like to express his appreciation to Korea Science and Engineering Foundation for partial financial support.

References

- [1] L.T. Canham, Porous semiconductors: a tutorial review, *Mat. Res. Soc. Symp. Proc* 452 (1997) 29–42.
- [2] I. Nozad, R.G. Carbonell, S. Whitaker, Heat conduction in multi-phase system. Part I: Theory and experiments for two-phase systems, *Chem. Engng. Sci* 40 (1985) 843–855.
- [3] T.H. Bauer, A general analytical approach toward the thermal conductivity of porous media, *Int. J. Heat Mass Transfer* 36 (1993) 4181–4191.

- [4] S.L. Lee, J.H. Yang, Modelling of effective thermal conductivity for a nonhomogeneous anisotropic medium, *Int. J. Heat Mass Transfer* 41 (1998) 931–937.
- [5] M. Kaviani, *Principles of Heat Transfer in Porous Media*, 2nd ed, Springer-Verlag, New York, 1995.
- [6] K. Nishioka, T. Murayama, Y. Ono, Estimation of effective thermal diffusivity of porous solid using data for image processing, *ISIJ International* 36 (1996) 150–155.
- [7] K. Bakker, Using the finite element method to compute the influence of complex porosity and inclusion structures on the thermal and electrical conductivity, *Int. J. Heat Mass Transfer* 40 (1997) 3503–3511.
- [8] J.M. Ziman, *Electron and Phonons*, Oxford University Press, Oxford, 1960.
- [9] A. Drost, P. Steiner, H. Moser, W. Lang, Thermal conductivity of porous silicon, *Sensors and Materials* 7 (1995) 111–120.
- [10] G. Benedetto, L. Boarino, R. Spagnolo, Evaluation of thermal conductivity of porous silicon layers by a photoacoustic method, *Appl. Phys. A* 64 (1997) 155–159.
- [11] G. Gesele, J. Linsmeier, V. Drach, R. Arens-Fischer, Temperature-dependent thermal conductivity of porous silicon, *J. Phys. D: Appl. Phys* 30 (1997) 2911–2916.
- [12] S.S. Tsao, T.R. Guiling, M.J. Kelly, Porous silicon formation in $n^-/n^+/n^-$ doped structures, *J. Electrochem. Soc* 138 (1991) 1739–1743.
- [13] M.I.J. Beale, J.D. Benjamin, M.J. Uren, N.G. Chew, A.G. Cullis, An experimental and theoretical study of the formation and microstructure of porous silicon, *Journal of Crystal Growth* 73 (1985) 622–636.
- [14] R.L. Smith, S.D. Collins, Porous silicon formation mechanisms, *J. Appl. Phys* 71 (1992) R1–R22.
- [15] R.L. Smith, S.F. Chuang, S.D. Collins, A theoretical model of the formation morphologies of porous, *J. Electron. Mater* 17 (1988) 533–541.
- [16] A. Majumdar, Microscale heat conduction in dielectric thin films, *ASME Journal of Heat Transfer* 115 (1993) 7–16.
- [17] C.L. Tien, G. Chen, Challenges in microscale conductive and radiative heat transfer, *Journal of Heat Transfer* 116 (1994) 799–807.
- [18] G. Chen, Thermal conductivity and ballistic-phonon transport in the cross-plane direction of superlattices, *Physical Review B* 57 (1998) 14958–14973.
- [19] W.S. Capinski, H.J. Maris, Thermal conductivity of GaAs/AlAs superlattices, *Physica B* 219/220 (1996) 699–701.
- [20] X.Y. Yu, G. Chen, A. Verma, J.S. Smith, Temperature dependence of thermophysical properties of GaAs, AlAs periodic structure, *Appl. Phys. Lett* 67 (1995) 3554–3556.
- [21] S.M. Lee, D.G. Cahill, Thermal conductivity of Si–Ge superlattices, *Appl. Phys. Lett* 70 (1997) 2957–2959.
- [22] Y.S. Touloukian, R.W. Powell, C.Y. Ho, P.G. Klemens, *Thermophysical Properties of Matter*, IFI/Plenum Press, New York/Washington, 1970.
- [23] S.V. Patankar, *Numerical Heat Transfer and Fluid Flow*, Hemisphere, Washington, DC, 1980.
- [24] C.J. Kim, S.T. Ro, A block-correction aided strongly implicit solver for the five-point formulation of elliptic differential equations, *Int. J. Heat Mass Transfer* 38 (1995) 999–1008.
- [25] P.J. Schneider, Conduction, in: W.M. Rohsenow, J.P. Hartnett, E.N. Ganic (Eds.), *Handbook of Heat Transfer Fundamentals*, 2nd ed, McGraw-Hill, New York, 1985 (Chapter 4).
- [26] W.G. Vincenti, C.H. Kruger, *Introduction to Physical Gas Dynamics*, Robert Krieger, New York, 1977.
- [27] R. Siegel, J.R. Howell, *Thermal Radiation Heat Transfer*, Hemisphere, Washington, DC, 1992.
- [28] M.F. Modest, *Radiative Heat Transfer*, McGraw-Hill, New York, 1993.
- [29] K.D. Lathrop, Spatial differencing of the transport equation: positivity vs. accuracy, *J. Computational Phys* 4 (1968) 475–498.
- [30] W.A. Fiveland, The selection of discrete ordinate quadrature sets for anisotropic scattering, *HTD* 160 (1991) 89–96.
- [31] M.N. Ozisik, *Radiative Transfer and Interactions with Conduction and Convection*, Wiley, New York, 1973.
- [32] M. Asheghi, M.N. Touzelbaev, K.E. Goodson, Y.K. Leung, S.S. Wong, Temperature-dependent thermal conductivity of single-crystal silicon layers in SOI substrates, *ASME Journal of Heat Transfer* 120 (1998) 30–36.
- [33] E.T. Swartz, R.O. Pohl, Thermal boundary resistance, *Review of Modern Physics* 61 (1989) 605–668.
- [34] R.L. Smith, S.D. Collins, Generalized model for the diffusion-limited aggregation and Efen models of cluster growth, *Physical Review A* 39 (1989) 5409–5413.
- [35] M. Kaviani, *Principles of Heat Transfer*, Course Pack, University of Michigan, 1998.
- [36] M.G. Holland, Analysis of lattice thermal conductivity, *Physical Review* 132 (1963) 2461–2471.
- [37] M.I. Flik, B.I. Choi, K.E. Goodson, Heat transfer regimes in microstructures, *ASME Journal of Heat Transfer* 114 (1992) 666–674.
- [38] W.A. Fiveland, J.P. Jessee, Acceleration schemes for the discrete ordinates method, *Journal of Thermophysics and Heat Transfer* 10 (1996) 445–451.